Journal of Alloys and Compounds 522 (2012) 167–171

Contents lists available at SciVerse ScienceDirect

Journal of Alloys and Compounds

journal homepage: www.elsevier.com/locate/jallcom

Core–shell VPO_4/C anode materials for Li ion batteries: Computational investigation and sol–gel synthesis

Y. Zhang, X.J. Zhang, Q. Tang, D.H. Wu, Z. Zhou*

Key Laboratory of Advanced Energy Materials Chemistry (Ministry of Education), Institute of New Energy Material Chemistry, Nankai University, Tianjin 300071, China

ARTICLE INFO

Article history:
Received 14 August 2011
Received in revised form 25 January 2012
Accepted 25 January 2012
Available online 4 February 2012

Keywords:
VPO_4/C
Lithium-ion batteries
Core–shell
Anode materials

ABSTRACT

Pristine VPO_4 is a ground-state magnetic semiconductor, disclosed by density functional theory computations; therefore, core–shell VPO_4/C composites were proposed and prepared via a sol–gel route. X-ray diffraction confirms the phase of orthorhombic vanadium phosphate, and scanning electron microscopy and transmission electron microscopy show that VPO_4 particles are coated with amorphous carbon film of ~8 nm in thickness to form core–shell nanostructures. Galvanostatic charge/discharge and cyclic voltammetry tests demonstrate that both the initial and reversible lithium storage capacities of VPO_4 were apparently enhanced due to the carbon coating. Core–shell structures can effectively improve the electrochemical performances of phosphate-based Li-ion battery materials.

1. Introduction

Li ion batteries are extremely important power sources in current society due to their superior performances. In the anodes of commercial Li ion batteries, graphite-based materials are mostly used because of low cost and high safety. However, the theoretical capacity of graphite, the commonly used anode material, is only 372 mAh g^{-1} [1], much lower than those of transition-metal oxides [2]. However, oxide anode materials suffer from large volume changes during repetitive charge and discharge cycles, leading to poor cyclic stability and rate capability [3–8]. Therefore, alternatives for anode materials with higher capacity and longer cyclic life are being actively investigated.

As we know, the poor cyclic stability and rate capability result from the fact that the structure of most transition-metal oxides will collapse when they react with Li electrochemically. If larger anions, such as PO_4^{3-}, are substituted for O^{2-}, phosphates can offer 3D space for Li ions, and may stabilize the framework and alleviate the volume changes during the charge and discharge process. Kalaiselvi et al. [9] for the first time proposed the application of $LiFePO_4$ as an anode material in Li ion batteries, and its cyclic performances were further improved through Cu and Sn doping [10]. Later $ATiOPO_4$ [11–13] (A = K^+, Na^+, Li^+, or Rb^+) and $M_{0.5}TiOPO_4$ [12–14] (M = Ni^{2+}, Co^{2+}, Mn^{2+}, or Mg^{2+}) were exploited as anode materials for Li ion batteries. Ren et al. [15] also found that β-$LiVOPO_4$ presented a reversible capacity higher than 380 mAh g^{-1} during 30 cycles as the anode material for Li ion batteries, and speculated a conversion reaction mechanism for Li recycle, $V + Li_3PO_4 \leftrightarrow VPO_4 + 3Li^+ + 3e^-$. Therefore, VPO_4 can be directly used as the anode material other than $LiVOPO_4$.

The crystal structure of VPO_4 has been clarified [16,17]; however, till now, the electronic structure of VPO_4 has not been investigated computationally, which is the basic knowledge for the application as Li ion battery materials. Also, no one has explored VPO_4 as the anode material in Li ion batteries yet. In this work, density functional theory (DFT) computations were firstly employed to investigate the structural and electronic properties of VPO_4, and then core–shell VPO_4/C composites were synthesized through a sol–gel method, and their electrochemical Li storage performances were compared with pristine VPO_4. Core–shell nanostructures are very important for the improvement of Li ion battery materials [18].

2. Computational and experimental

2.1. Computational details

DFT computations were performed by using the plane-wave technique implemented in the Vienna ab initio simulation package (VASP). The ion-electron interaction is described with the projector augmented wave (PAW) method [19]. The exchange-correlation potential is approximated by the generalized gradient approximation (GGA) using the PW91 functional [20] for both spin-polarized and spin-unpolarized cases. An energy cutoff of 360 eV and an appropriate *k*-point mesh (5 × 5 × 5) were chosen for the geometry optimization, and the total ground state energy was converged to within 3 meV per formula unit. Pseudopotentials with $3p^6 3d^4 4s^1$,

* Corresponding author. Tel.: +86 22 23503623; fax: +86 22 23498941.
E-mail address: zhouzhen@nankai.edu.cn (Z. Zhou).

0925-8388/$ – see front matter © 2012 Elsevier B.V. All rights reserved.
doi:10.1016/j.jallcom.2012.01.143

$2s^2 2p^4$, and $3s^2 3p^3$ valence electron configurations were used for V, O, and P atoms, respectively. Since GGA usually underestimates the band gap of transition metal compounds, we applied a more accurate GGA+U approach [21] which allows a better description of the electronic correlation with regard to the *d*-orbitals of transition metal atoms. For GGA+U approach, a U value of 4.5 eV was suggested to correct the electronic correlation. Additionally, we also used the Heyd–Scuseria–Ernzerhof (HSE) screened exchange hybrid functional [22,23], which has proven to give quantitatively accurate band gaps, to examine the band structure of bulk VPO_4.

2.2. Sample preparation

The VPO_4/C composite was obtained through a sol–gel route. The starting materials, V_2O_5 and $H_2C_2O_4$ in stoichiometric amount (Eq. (1)), were dissolved in distilled water with stirring at 70 °C for 1 h, and then a glaucous sol formed. In this procedure, V(V) was reduced to V(IV). In addition, stoichiometric amount of $NH_4H_2PO_4$ (Eq. (2)) was added to the above sol while being stirred at 70 °C for 4 h to form a gel slowly. After the gel was dried in an oven at 100 °C for 12 h, the resulting powder was pressed into pellets. The pellets were initially heated at 350 °C for 4 h in Ar atmosphere, and then glucose (VPO_4:C = 100:5) was added to the powder and mixed uniformly. Finally VPO_4/C was obtained after the mixture was calcined at 750 °C for 12 h in Ar atmosphere. The pristine VPO_4 free of carbon was prepared through the same procedures except the glucose addition.

$$V_2O_5 + 3H_2C_2O_4 \rightarrow 2VOC_2O_4 + 3H_2O + 2CO_2 \quad (1)$$

$$2VOC_2O_4 + 2NH_4H_2PO_4 \rightarrow 2VPO_4 + 3CO_2 + CO + 2NH_3 + 3H_2O \quad (2)$$

2.3. Material characterization

The sample was identified by X-ray diffraction (XRD) under the Rigaku D/MAX III diffractometer with a Cu Kα radiation (k = 1.5418 Å). The grain size and morphology were observed by using a Hitachi S–3500N scanning electron microscopy (SEM). The microstructure was also observed through a FEI Tecnai 20 transmission electron microscopy (TEM). The Raman spectrum was collected at room temperature by using a RFS100–S spectrometer equipped with a 1064 nm laser excitation. The amount of carbon was tested by virio-EL C H N elemental analyzer.

2.4. Electrochemical tests

Electrochemical measurements were conducted in Li test cells with lithium foil as counter and reference electrodes. All the test cells contained 1.0 mol L^{-1} $LiPF_6$ in ethylene carbonate (EC)–ethyl methyl carbonate (EMC)–dimethyl carbonate (DMC) (1:1:1 in volume) as electrolyte. The active material, carbon black, and polytetrafluoroethylene (PTFE) binder were mixed at a weight ratio of 85:10:5, and then rolled into sheets. The sheets were cut into circular strips of 8 mm in diameter on the Cu foil. The strips were dried at 100 °C for 12 h. The galvanostatic charge/discharge cycling tests were performed in a voltage range of 0.01–3.0 V within Land battery testers. Cyclic voltammetry (CV) was carried out on a CHI 600A electrochemical analyzer with a scan rate of 0.1 mV s^{-1} in the potential range of 0.01–3.0 V (vs. Li/Li^+).

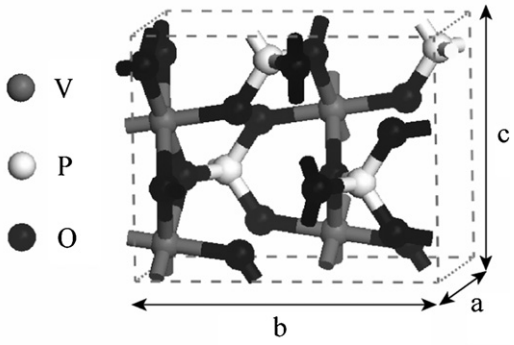

Fig. 1. Optimized crystal structure of VPO_4 with a unit cell.

3. Results and discussion

3.1. Geometric and electronic structure of VPO_4

The optimized crystal structure of VPO_4 with the unit cell is presented in Fig. 1. The unit cell is composed of four formula units of this compound. The O atoms form a nearly tetrahedral arrangement around each P site and an approximately octahedral arrangement around each V site. The relaxed lattice parameters are summarized in Table 1. Compared with the experimental values (in this work and Ref. [16]), the relaxation shows a shrink within 1% error along the three lattice orientations, which is common for DFT computations.

Furthermore, our computations indicate that the ground state of VPO_4 adopts a magnetic configuration. The magnetic energy gain, defined as the difference in the total energy of ferromagnetic configuration vs. the total energy of the spin non-polarized configuration, is ~0.516 eV per formula unit. To understand the possible impact of magnetic structure, we calculated the total energy of both the ferromagnetic (FM) and anti-ferromagnetic (AFM) orderings. The AFM state is slightly more stable than the FM state with a small energy difference less than 0.006 eV per formula unit. This is in good agreement with the result experimentally determined low-temperature AFM ordering by Glaum et al. [16]. Note that the low-temperature magnetic state of VPO_4 is non-collinear and prone to become magnetically disordered at higher temperatures. On the other hand, the energy difference between FM and AFM state is so small that most of the interest in this material is focused on the room-temperature behaviors which have no spin ordering. For clarity, the electronic structure calculation of this material is approximately represented by the FM ordering. Actually the FM approximate treatment can also be found in $LiFePO_4$ and $LiMnPO_4$ [24]. The partial density of states (DOS) and band structure of VPO_4 in the ferromagnetic configuration are plotted in Figs. 2 and 3, respectively. The states associated with V atoms are primarily of 3d character and the states associated with O atoms are mainly of 2p character. Clearly, the V—O bonding orbital is largely attributed to the hybridization of V 3d states and O 2p states throughout the valence band range. The lower valence band is mostly due to O 2p states while the conduction band is mostly contributed by V 3d states. Moreover, the occupied minority spin has a smaller

Table 1
Optimized and experimental lattice parameters of VPO_4 in the orthorhombic structure.

	a (Å)	*b* (Å)	*c* (Å)
GGA+U	5.181	7.738	6.214
Ref. [16]	5.232	7.774	6.285
Experimental in this work	5.228	7.786	6.277

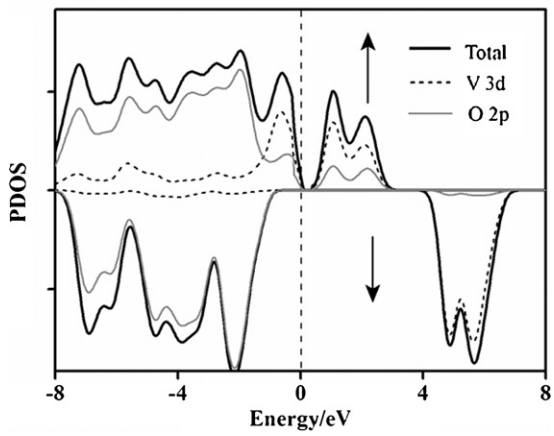

Fig. 2. Density of states (DOS) of VPO_4 in the ferromagnetic state. The upper and lower part are related to the majority (↑) and minority (↓) state, respectively. The partial states of V_{3d} and O_{2p} are shown together with the total DOS.

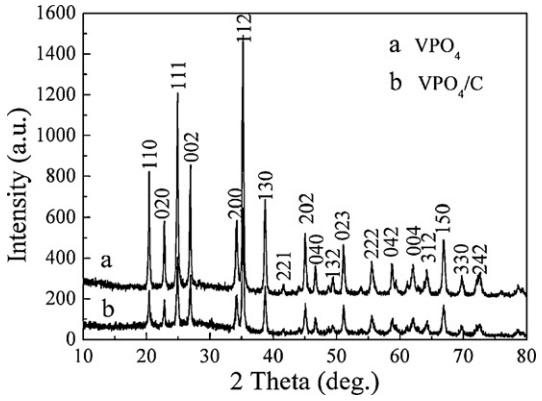

Fig. 4. XRD patterns of pristine VPO_4 and VPO_4/C composite.

contribution from V 3d orbital than the majority state. The band structure in Fig. 3a characterizes VPO_4 crystal as a ferromagnetic semiconductor with a band gap of 0.95 eV. The conduction band minimum is located at the Γ point, and the conduction band is composed of the anti-bonding P—O and V—O orbitals. Since the GGA + U method usually underestimates the band gap, we recomputed the band structure from HSE functional (Fig. 3b), and the band gap is increased to 2.91 eV, larger than the GGA + U result; however, the basic physical nature remains reliable within the GGA + U framework. Our DFT results reveal that VPO_4 has magnetic semiconducting ground state. As other phosphate Li ion battery materials, here we proposed to improve the room-temperature electrical conductivity of VPO_4 by carbon coating.

3.2. Material characterization

The XRD patterns of pristine VPO_4 and VPO_4/C composite are shown in Fig. 4. Both samples can be indexed to an orthorhombic structure with the space group *CmCm* and there are no impurities that can be detected from the patterns. There are also no diffraction peaks for crystalline carbon (graphite) [25], which is probably due to the fact that the carbon content is rather low or most of the carbon in the VPO_4/C composite is amorphous. The existence of carbon can be revealed from the following TEM image and Raman spectrum. Elemental analysis shows that the amount of carbon in the sample is about 2.8 wt%.

The SEM images of VPO_4 and VPO_4/C composite are presented in Fig. 5a and b, respectively. Both of them exhibit irregular shape with some aggregation. The VPO_4/C particles do not become larger obviously after the carbon coating. Fig. 5c clearly reveals the coexistence of two phases, VPO_4 and amorphous carbon. The primary crystallite is completely coated with a carbon shell which is ~8 nm in thickness. The dark region is VPO_4 crystallite as a core, and the light shade is carbon coating as a shell, similar to core–shell $LiCoPO_4$/C [26], $Li_3V_2(PO_4)_3$/C [27], $LiFe_{1/3}Mn_{1/3}Co_{1/3}PO_4$/C [28], and $Ni_{0.5}TiOPO_4$/C [29] composites. Fig. 5d shows the Raman spectrum for VPO_4/C composite. The two peaks around 1300 and 1590 cm^{-1} correspond to the D and G band, respectively. The coexistence of D- and G-band (I_D/I_G = 0.85) indicates the part crystallization of carbon in VPO_4/C composites [30–33].

3.3. Electrochemical tests

The discharge behaviors of VPO_4 and VPO_4/C anodes are disclosed in Fig. 6a between 0.01 and 3.0 V at the current density of 20 mA g^{-1}. Although the coating carbon can react with Li ions during the charge–discharge cycles, the results reported here removed the contribution of carbon, by testing the electrochemical performances at the same conditions of the electrodes with only the pyrolyzed carbon from glucose as the active materials. During the first discharge, the VPO_4/C and VPO_4 anodes deliver a capacity of 887.3 and 548.7 mAh g^{-1}, respectively, while the capacities for the second discharge remain 502.0 and 321.3 mAh g^{-1}, respectively. As the theoretical capacity of VPO_4 is 551 mAh g^{-1} [15], the irreversible capacity in the first cycle can be attributed to the decomposition of the electrolyte and the formation of the solid electrolyte interphase (SEI) films [34]. As Fig. 6b shows, Li_2O (the

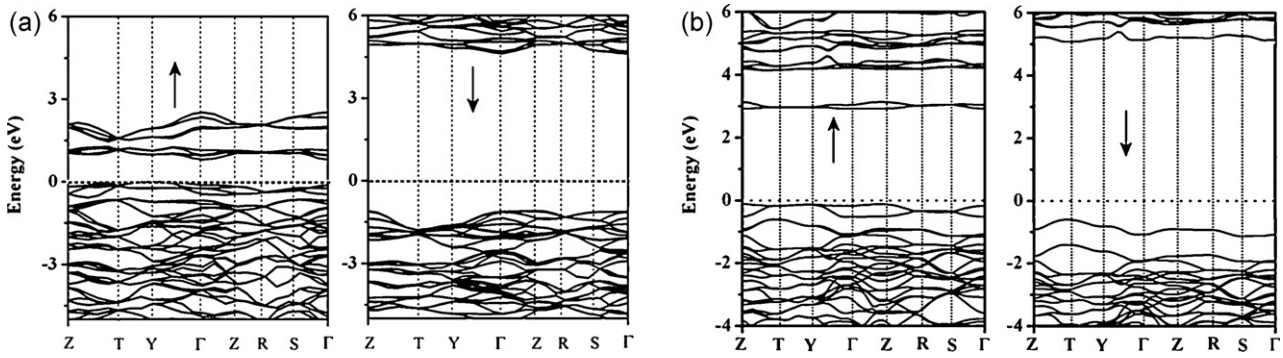

Fig. 3. Band structure of VPO_4 in the ferromagnetic configuration for the majority state (↑) and minority state (↓). The Fermi-level is represented by a dashed line. (a) and (b) were computed from GGA + U and HSE, respectively.

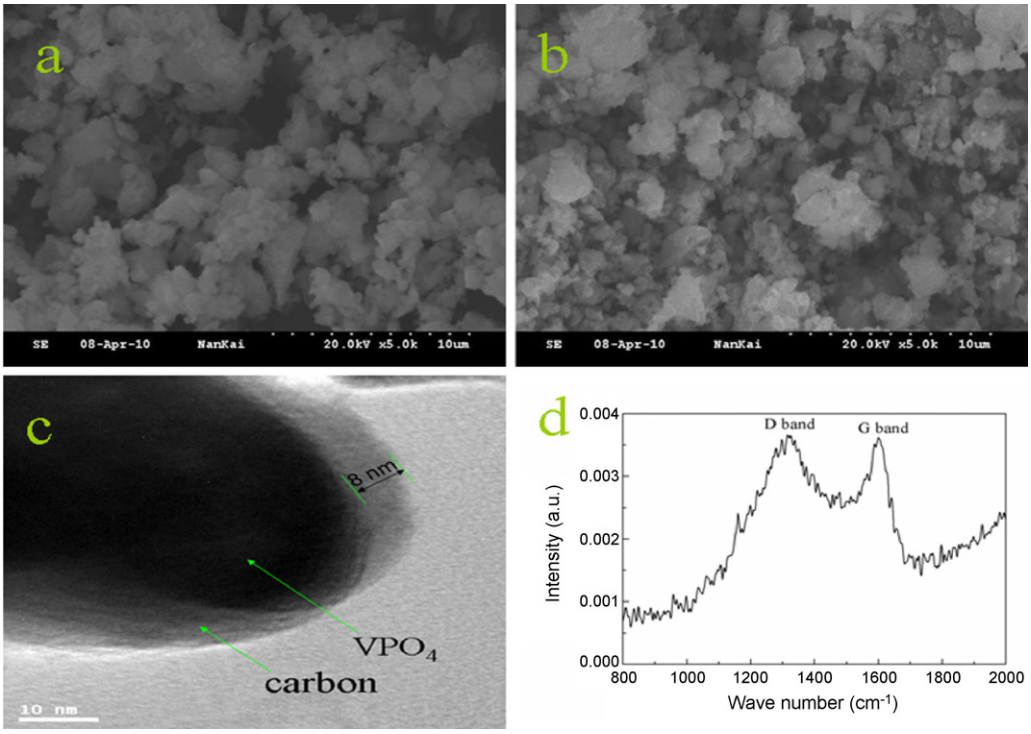

Fig. 5. SEM images of VPO_4 (a), VPO_4/C composite (b), (c) is the TEM image, and (d) is the Raman spectrum of VPO_4/C composite.

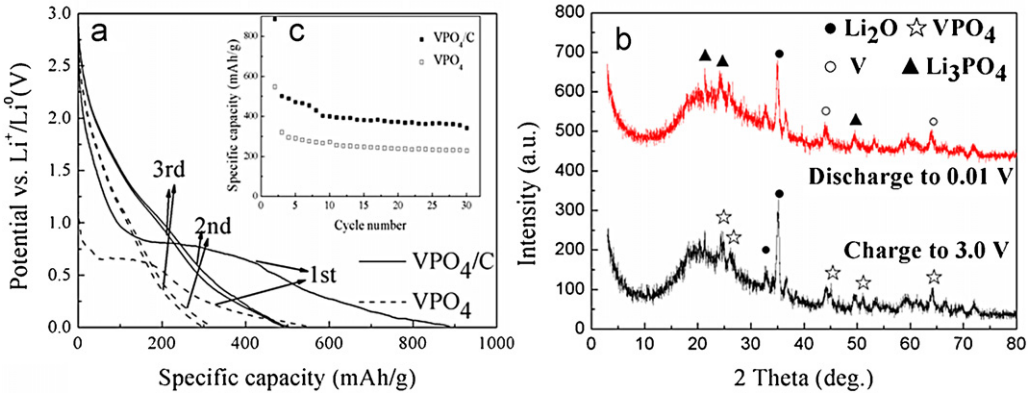

Fig. 6. Initial three discharge curves (a) and cyclic performance (c) for VPO_4 and VPO_4/C at the current density of 20 mA/g. XRD patterns (b) of the VPO_4 electrode during the first cycle at the charged state (3.0 V) and discharged state (0.01 V).

main chemical component of the SEI films) and V were generated when discharged to 0.01 V. After charged to 3.0 V, V was transformed into VPO_4 again. This reversible reaction process can be interpreted by Eq. (3): there are three lithium ions to react with VPO_4 reversibly, similar to the mechanism proposed in previous reports [15,35]. The cyclic performances of VPO_4 and VPO_4/C are compared in Fig. 6c. After 30 cycles, the discharge capacities remain 343.0 and 230.1 mAh g^{-1} for VPO_4/C and VPO_4 anode, respectively. The discharge capacities and the cyclic stability are improved due to the carbon coating.

$$V + Li_3PO_4 \leftrightarrow VPO_4 + 3Li^+ + 3e^- \quad (3)$$

Fig. 7 shows the initial three-cycle CV profiles of VPO_4 and VPO_4/C with a potential range 0.01–3.0 V at a scan rate of 0.1 mV s^{-1}. The peak profiles of VPO_4/C are sharper than those of pristine VPO_4 except the first cycle, because the decomposition of the electrolyte and the formation of the SEI films are more severe in the pristine one. This indicates that the carbon coating enhanced the reversibility and cyclic stability of the electrode. As shown in Fig. 7, we also observe that the subsequent cycles are similar but different from the first cycle. This reveals that the decomposition of the electrolyte and the formation of the SEI films during the first cycle are irreversible, while the subsequent cycles are reversible as described in Eq. (3), in agreement with the galvanostatic charge/discharge results. The CV profiles indicate that part of the capacity of the electrodes is ascribable to non-faradic phenomena. This behavior has been observed in other conversion oxysalts different from phosphates recently described in the literature as 'conversion' materials [36,37].

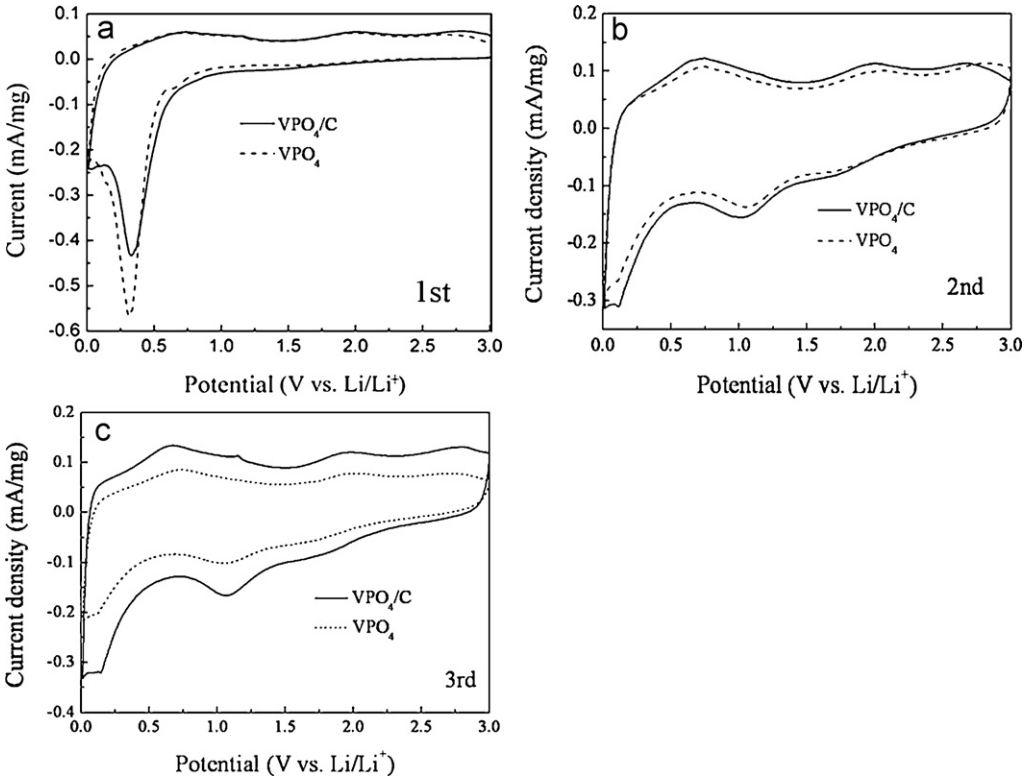

Fig. 7. The initial three-cycle CV curves of VPO_4 and VPO_4/C.

4. Conclusions

Density functional theory computations disclose that pristine VPO_4 is a magnetic semiconductor. Similar to other phosphate compounds, we proposed core–shell VPO_4/C composites for the purpose of utilizing this compound as anode materials of Li ion batteries. Core–shell VPO_4/C composites were realized experimentally through a sol–gel route and subsequent calcination with glucose as carbon source, and were explored as anode materials for lithium ion batteries. TEM analysis clearly shows a carbon layer with the thickness of ~8 nm coating in the surfaces of VPO_4. The initial discharge capacity of VPO_4/C is as high as 887.3 mAh g^{-1} and remains 343.0 mAh g^{-1} after 30 cycles, much higher than those of pristine VPO_4. Large PO_4^{3-}can stabilize the structure and may alleviate the change of the cell volume during charge and discharge cycles. Furthermore, carbon shells in the composites optimize the electrochemical performances of phosphate electrode materials. Therefore, core–shell phosphate/C composites are worth extensively exploiting as anode materials for lithium ion batteries.

Acknowledgment

This work was supported by the 973 Program (2009CB220100) in China.

References

[1] B. Scrosati, Electrochim. Acta 45 (2000) 2461.
[2] P. Poizot, S. Laruelle, S. Grugeon, L. Dupont, J.M. Tarascon, Nature 407 (2000) 496.
[3] J. Zhong, X.L. Wang, X.H. Xia, C.D. Gu, J.Y. Xiang, J. Zhang, J.P. Tu, J. Alloys Compd. 509 (2011) 3889.
[4] Y. Qi, N. Du, H. Zhang, J.Z. Wang, Y. Yang and D.R. Yang, J. Alloys Compd. (2012) doi:10.1016/j.jallcom.2012.01.046.
[5] N. Sivakumar, S.R.P. Gnanakan, K. Karthikeyan, S. Amaresh, W.S. Yoon, G.J. Park, Y.S. Lee, J. Alloys Compd. 509 (2011) 7038.
[6] L.C. Yang, W.L. Guo, Y. Shi, Y.P. Wu, J. Alloys Compd. 501 (2010) 218.
[7] S.M. Lee, H.S. Kim, T.Y. Seong, J. Alloys Compd. 509 (2011) 3136.
[8] F. Wang, W. Tao, M. Zhao, M. Xu, S. Yang, Z. Sun, L. Wang, X. Song, J. Alloys Compd. 509 (2011) 9798.
[9] N. Kalaiselvi, C.H. Doh, C.W. Park, S.I. Moon, M.S. Yun, Electrochem. Commun. 6 (2004) 1110.
[10] N. Jayaprakash, N. Kalaiselvi, Electrochem. Commun. 9 (2007) 620.
[11] G.D. Stucky, M.L.F. Phillips, T.E. Gier, Chem. Mater. 1 (1989) 492.
[12] I. Belharouak, A. Khalil, Electrochem. Commun. 7 (2005) 648.
[13] M. Chakir, A.E. Jazouli, J.P. Chaminade, F. Bourée, D.d. Waal, Mater. Res. Bull. 42 (2007) 1348.
[14] R. Essehli, B.E. Bali, H. Ehrenberg, I. Svoboda, N. Bramnik, H. Fuess, Mater. Res. Bull. 44 (2009) 817.
[15] M.M. Ren, Z. Zhou, X.P. Gao, J. Appl. Electrochem. 40 (2010) 209.
[16] R. Glaum, M. Reehuis, N. Stüsser, U. Kaiser, F. Reinauer, J. Solid-State Chem. 126 (1996) 15.
[17] E.J. Baran, F. Muto, N. Kumada, N. Kinomura, J. Mater. Sci. Lett. 11 (1989) 1305.
[18] L.W. Su, Y. Jing, Z. Zhou, Nanoscale 3 (2011) 3967.
[19] J.P. Perdew, J.A. Chevary, S.H. Vosko, K.A. Jackson, M.R. Pederson, D.J. Singh, C. Fiolhais, Rev. B 46 (1992) 6671.
[20] P.E. Blöchl, Phys. Rev. B 50 (1994) 17953.
[21] F. Zhou, Phys. Rev. B 70 (2004) 235121.
[22] J. Heyd, G.E. Scuseria, M. Ernzerhof, J. Chem. Phys. 118 (2003) 8207.
[23] J. Heyd, G.E. Scuseria, J. Chem. Phys. 121 (2004) 1187.
[24] F. Zhou, K. Kang, T. Maxisch, G. Ceder, D. Morgan, Solid State Commun. 132 (2004) 181.
[25] S.S. Zhang, J.L. Allen, K. Xu, T.R. Jow, J. Power Sources 147 (2005) 234.
[26] H.H. Li, J. Jin, J.P. Wei, Z. Zhou, J. Yan, Electrochem. Commun. 11 (2009) 95.
[27] M.M. Ren, Z. Zhou, X.P. Gao, W.X. Peng, J.P. Wei, J. Phys. Chem. C 112 (2008) 5689.
[28] Y. Zhang, C.S. Sun, Z. Zhou, Electrochem. Commun. 11 (2009) 1183.
[29] X.J. Zhang, Y. Zhang, Z. Zhou, J.P. Wei, R. Essehli, B. Elbali, Electrochim. Acta 56 (2011) 2290.
[30] L.W. Su, Z. Zhou, M. Ren, Chem. Commun. 46 (2010) 2590.
[31] S.M. Yuan, J.X. Li, L.T. Yang, L.W. Su, L. Liu, Z. Zhou, ACS Appl. Mater. Interfaces 3 (2011) 705.
[32] S.M. Yuan, Z. Zhou, G. Li, CrystEngComm 13 (2011) 4709.
[33] H. Kim, J. Cho, J. Electrochem. Soc. 154 (2007) A462.
[34] H. Liu, G. Wang, J. Wang, D. Wexler, Electrochem. Commun. 10 (2008) 1879.
[35] C.Y. Ouyang, S.Q. Shi, Q. Fang, M.S. Lei, J. Power Sources 175 (2008) 891.
[36] M.J. Aragón, B. León, C.P Vicente, J.L. Tirado, Chem. Mater. 21 (2009) 1834.
[37] M.J. Aragón, B. Leoîn, T. Serrano, C.P. Vicente, J.L. Tirado, J. Mater. Chem. 21 (2011) 10102.